Modelling and analysis of a direct methanol fuel cell with under-rib mass transport and two-phase flow at the anode

Yuming Yang, Yung C. Liang*

Department of Electrical and Computer Engineering, National University of Singapore, Kent Ridge, Singapore 119260, Republic of Singapore

A R T I C L E   I N F O

A B S T R A C T

For the past decade, extensive mathematical modelling has been conducted on the design and optimization of liquid-feed direct methanol fuel cells (DMFCs). Detailed modelling of DMFC operations reveals that a two-phase flow phenomenon at the anode and under-rib convection due to the pressure difference between the adjacent channels both contribute significantly to mass-transfer in a DMFC and its output performance. In practice, comprehensive simulations based on the finite volume technique for two-phase flow require a high level of numerical complexity in computation. This study presents a complexity-reduced mathematical model that is developed to cover both phenomena for a realistic, but fast, in computation for the prediction and analysis of a DMFC prototype design. The simulation results are validated against experimental data with good agreement. Analysis of the DMFC mass-transfer is made to investigate methanol distribution at anode and its crossover through the proton-exchange membrane. From a comparison of the influence of two-phase flow and under-rib mass-transfer on DMFC performance, the significance of gas-phase methanol transport is established. Simulation results suggest that both the optimization of the flow-field structure and the fuel cell operating parameters (flow rate, methanol concentration and operating temperature) are important factors for competitive DMFC performance output.

1. Introduction

The direct methanol fuel cell (DMFC) is considered to be a promising-next generation power source, especially for portable and micro-scale applications, due to its simplicity, low temperature operation, and relatively high specific energy [1,2]. Nevertheless, the present performance of DMFCs is interior to that of state-of-the-art lithium-ion batteries. The key barriers to its rapid commercialization are poor methanol oxidation kinetics and methanol crossover through the polymer membrane [3,4]. Although extensive research is being conducted world-wide on new materials for performance improvement, other work on DMFC design and optimization using currently available materials emerge is also an important topic [5]. The availability of a mathematical model of a DMFC helps to understand the interactions inside the cell. Furthermore, a model serves as a tool to optimize DMFC design and allows more accurate prediction of the performance before a prototype is made [6]. Therefore, a good mathematical model is essential for the design and development of a competitive DMFC.

In the development of DMFC models, the mass transport of reactants has been found to be an important and crucial issue. Accordingly, their parameter has attracted more attention in model development [7,8]. In early work, only single-phase mass transport in one or two dimensions was adopted in models [9–13]. The typical assumption, such as specified in the models by Meyers and Newman [9–11] and Baxter et al. [12], was that carbon dioxide produced in the reaction remains fully dissolved in the liquid fuel. This assumption was found to be inadequate by studies of the flow visualization of carbon dioxide growth and its ejection from the diffusion layer [14–17]. Therefore, unlike other types of fuel cell, methanol transport in a DMFC occurs in a liquid–gas two-phase flow, which consists of aqueous methanol and gaseous carbon dioxide. Accordingly, the mass transport process is more complex and it makes the development of a two-phase model rather challenging. Wang and Wang [18–20] successfully simulated the two-phase flow and transport in a DMFC by applying their multiphase mixture (M^2) flow model. Capillary action was believed to be the dominant mechanism for two-phase flow within the diffusion layer. The simulation clearly showed the effect of the gas phase transport of methanol on the DMFC output performance. Thus, two-phase flow is

---

Nomenclature

Symbols

C	molar concentration ($mol\,cm^{-3}$)
D	diffusion coefficient ($cm^2\,s^{-1}$)
d_h	hydraulic diameter (cm)
F	Faraday constant ($96,487\,A\,s\,mol^{-1}$)
h_m	mass-transfer coefficient between channel and diffusion layer ($cm\,s^{-1}$)
I_{cell}	current density ($A\,cm^{-2}$)
j	current density per unit volume ($A\,cm^{-3}$)
K	proportional coefficient for methanol electro-osmosis drag coefficient
k	permeability of porous materials (cm^2)
k_H	Henry's law constant (Pa)
l	channel length (cm)
M	molecular weight ($g\,mol^{-1}$)
N	mass flux ($mol\,(cm^2\,s)^{-1}$)
$n_{EOD}^{H_2O}$	water electro-osmosis drag coefficient ($cm^3\,mol^{-1}$)
P_{inlet}	inlet flow pressure (Pa)
P	pressure (Pa)
ΔP	pressure drop (Pa)
R	universal gas constant ($8.314\,J\,mol^{-1}\,K^{-1}$)
$R_{contact}$	ohmic contact resistance ($\Omega\,cm^2$)
S	liquid saturation
Sh	Sherwood number
T	temperature (K)
V_{cell}	cell voltage (V)
v	flow velocity ($cm\,s^{-1}$)
x	coordinate along channel (cm)
y	coordinate across channel to membrane (cm)

Superscripts

$MeOH$	methanol
CO_2	carbon dioxide
H_2O	water
O_2	oxygen

Subscripts

A	anode
C	cathode
CH	channel
$CH–DL$	channel to diffusion layer
Cov	convection
DL	diffusion layer
$Diff$	diffusion
EOD	electro-osmosis drag
eff	effective value
g	gas phase
in	inlet
l	liquid phase
m	membrane
ref	reference value
sat	saturated
$U\text{-}rib$	under-rib
V	vapor

Greek letters

α_A	anodic transfer coefficient at anode
α_C	cathodic transfer coefficient at cathode
α	gas void fraction in channel
η	overpotential (V)
ε	porosity
τ	tortuosity factor
κ_m	proton conductivity of PEM ($S\,cm^{-1}$)
σ	interfacial tension ($S\,cm^{-1}$)
μ_A	viscosity ($kg\,(cm\,s)^{-1}$)

ρ　　　density $(g\,cm^{-3})$
χ_{EOD}^{MeOH}　　methanol electro-osmosis drag coefficient $(cm^3\,mol^{-1})$
χ_l^{MeOH}　　liquid methanol molar fraction

recognized to be a more realistic model for mass transport in DMFCs [21–25]. The effect on mass-transfer by under-rib convection within the diffusion layer was also investigated extensively, although mostly in hydrogen proton-exchange membrane fuel cells (H_2 PEMFCs) [26–31]. Under-rib convection is induced by the pressure drop between two adjacent channels. It is understood that such convection dominates lateral species transport in the diffusion layer. Recently, under-rib mass transport was found to have a substantial influence on DMFC performance [7,32].

Most of the available mathematical models are applied numerically using the finite volume technique, together with the computable fluidic dynamics (CFD) method. Detailed analysis on the species transport is made by the complete Navier–Stokes equation set, but involves vast numerical complexity.

In this study, a concise mathematical model is developed for quick numerical simulation to allow performance prediction and analysis of a DMFC. Two-phase flow at the anode and pressure-driven convection are both included in the proposed model and thereby enable accurate and realistic performance prediction and analysis. The results are validated by laboratory measurement data.

2. Mathematical model

A schematic of a DMFC with a single serpentine channel (SSC) is shown in Fig. 1. The anode and cathode sides have a similar structure that consists of a fuel channel and diffusion layer. A Nafion® type proton-exchange membrane (PEM) is sandwiched between the anode and the cathode, with catalysts supported on carbon particles on each side for the fuel cell reactions, namely methanol oxidation on a platinum–ruthenium (Pt–Ru) alloy at the anode and oxygen reduction on a platinum (Pt) at the cathode. The electrocatalytic reaction at the anode can be expressed as
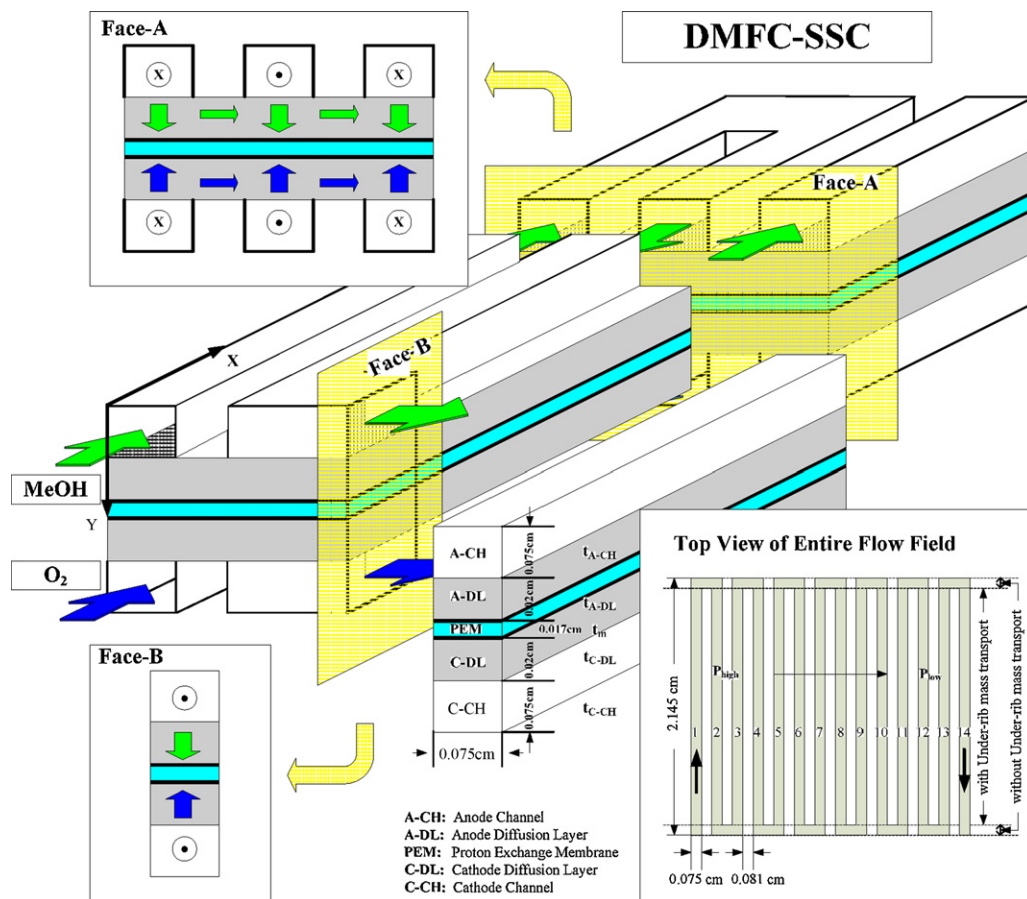
$$CH_3OH + H_2O \rightarrow CO_2 + 6H^+ + 6e^-\qquad(1)$$

Fig. 1. Schematic structure of DMFC with SSC pattern for both sides. Face A represents a cross-sectional view of region with under-rib mass transport. Face B represents the region without under-rib mass transport.

and the reaction at cathode is

$$6H^+ + 6e^- + 1.5O_2 \rightarrow 3H_2O \tag{2}$$

For simplicity, both catalyst layers are assumed to be infinitely thin at the interface between the diffusion layer and the PEM in the proposed model. Accordingly, the methanol/oxygen diffusion with electrochemical reaction is assumed ideal in these layers. The modelling work on cell performance and mass transport therefore addresses the flow channel, diffusion layer and PEM regions.

The SSC is treated in two regions for mass transport analysis, as shown in the top-view of the entire flow-field in Fig. 1. The under-rib convection mass flux takes place between neighboring channels. In this region, species flux is not only driven by the concentration gradient, but also by the pressure difference between channels according to Darcy's convection flow. The liquid pressure in the cross-section is assumed to be homogeneous in the channel and beneath diffusion layer. For the region with a horizontal short turning of flow channel, the mass flux is assumed to be driven mainly by the concentration gradient and the convection flux can be neglected due to the relatively small pressure drop along the channel. The phenomenon is indicated in the cross-sectional view of face B in Fig. 1. The two-phase mixture flow is the main transport mode for methanol and carbon dioxide at anode. In the anode channel region, the laminar two-phase flow is treated homogeneously and similar gas and liquid phase velocities are maintained. At the cathode, the two-phase effect is not considered due to the very small amount of liquid water [18]. The crossover of methanol through the PEM from the anode to the cathode is assumed to be oxidized instantaneously at the cathode catalyst layer [33,34].

Other assumptions for the mass transport in the model development are: (1) all processes in the DMFC system are isothermal and under a steady-state condition; (2) the liquid and gas considered in the model are incompressible and their flows are laminar due to the low Reynolds number; (3) porous diffusion layers are isotropic and homogeneous and characterized by effective porosity and permeability.

2.1. Methanol crossover in PEM

In a PEM, the crossover methanol flux arises in the presence of excessive un-reacted methanol at the diffusion layer|PEM interface due to slow methanol oxidation kinetics. The crossover is driven by diffusion under a concentration gradient, electro-osmosis drag proportional to cell current density and local methanol concentration, as well as a pressure difference and local methanol concentration induced convection across the PEM [35], i.e.,

$$N_m^{MeOH} = -D_{m,eff}^{MeOH} \frac{dC_m^{MeOH}}{dy_m} + \chi_{EOD}^{MeOH} C_m^{MeOH} \frac{I_{cell}}{F} - k_m^p C_m^{MeOH} \frac{\Delta P_m}{t_m} \tag{3}$$

where the methanol electro-osmosis drag coefficient is $\chi_{EOD}^{MeOH} = K_{EOD} n_{EOD}^{H_2O}$ and the effective diffusion coefficient is $D_{m,eff}^{MeOH} = (\varepsilon_m)^{\tau_m} D_l^{MeOH}$, respectively.

The flux is constant in the PEM at steady state and therefore the methanol concentration distribution can be solved with the boundary conditions of $C_m^{MeOH} = C_{A-DL}^{MeOH}\big|_{y=t_{A-DL}}$ at the interface between anode catalyst layer and PEM, and $C_m^{MeOH} = 0$ at the cathode catalyst layer assuming that all crossover methanol molecules are consumed by combination with oxygen at cathode side; i.e.,

$$C_m^{MeOH} = C_{A-DL}^{MeOH}\big|_{y=t_{A-DL}} \frac{\exp((\Gamma_A^1/D_{m,eff}^{MeOH})y_m) - \exp((\Gamma_A^1/D_{m,eff}^{MeOH})t_m)}{1 - \exp((\Gamma_A^1/D_{m,eff}^{MeOH})t_m)}, \quad \Gamma_A^1 = \chi_{EOD}^{MeOH} \frac{I_{cell}}{F} - k_m^p \frac{\Delta P_m}{t_m} \tag{4}$$

Therefore, the crossover methanol flux in PEM is given as

$$N_m^{MeOH} = C_{A-DL}^{MeOH}\big|_{y=t_{A-DL}} \Gamma_A^1 \frac{\exp((\Gamma_A^1/D_{m,eff}^{MeOH})t_m)}{\exp((\Gamma_A^1/D_{m,eff}^{MeOH})t_m) - 1} \tag{5}$$

Accordingly, the diffusion, electro-osmosis drag, as well as convection partial flux are

$$\begin{cases} N_{m,Diff}^{MeOH} = -C_{A-DL}^{MeOH}\big|_{y=t_{A-DL}} \Gamma_A^1 \dfrac{\exp((\Gamma_A^1/D_{m,eff}^{MeOH})t_m)}{1 - \exp((\Gamma_A^1/D_{m,eff}^{MeOH})t_m)} \\[3ex] N_{m,EOD}^{MeOH} = -\chi_{EOD}^{MeOH} \dfrac{I_{cell}}{F} C_{A-DL}^{MeOH}\Big|_{y=t_{A-DL}} \dfrac{\exp((\Gamma_A^1/D_{m,eff}^{MeOH})t_m) - \exp((\Gamma_A^1/D_{m,eff}^{MeOH})t_m)}{1 - \exp((\Gamma_A^1/D_{m,eff}^{MeOH})t_m)} \\[3ex] N_{m,Cov}^{MeOH} = -k_m^p \dfrac{\Delta P_m}{t_m} C_{A-DL}^{MeOH}\Big|_{y=t_{A-DL}} \dfrac{\exp((\Gamma_A^1/D_{m,eff}^{MeOH})y_m) - \exp((\Gamma_A^1/D_{m,eff}^{MeOH})t_m)}{1 - \exp((\Gamma_A^1/D_{m,eff}^{MeOH})t_m)} \end{cases} \tag{6}$$

2.2. Methanol mass transport at anode

At the anode, methanol solution is supplied from the anode flow channel. It is treated differently with and without under-rib convection in the corresponding region, as follows.

2.2.1. Under-rib mass transport region

In the region with under-rib mass transport, the Darcy-type methanol flow consists of diffusion flux and a convection under-rib flux governed by the Darcy model, i.e.,

$$N_{A-DL}^{MeOH} = -D_{A-DL,eff}^{MeOH} \frac{dC_{A-DL}^{MeOH}}{dy_{A-DL}} - \frac{k_{A-DL}^p}{\mu_A} C_{A-DL}^{MeOH} \frac{\Delta P_{U-rib}}{l_h} \tag{7}$$

The effective diffusion coefficient of methanol $D_{A-DL,eff}^{MeOH}$ in the layer also relates to the porosity and tortuosity of the porous region similar to that in the PEM. Mixed parameters, which will be elaborated in the two-phase section below, will be applied assuming that methanol is transported in both the gas and the liquid phases in the diffusion layer.

The pressure drop ΔP_{U-rib} in the above flux expression is the difference in the local pressure at corresponding points between adjacent channels. Assuming laminar flow in the fuel channel, this pressure drop of methanol flow along channel can be derived from laminar flow theory [36], i.e.,

$$\Delta P_{A-CH}(x) = \frac{32 v_{A-CH} \mu_A}{d_h^2} x \tag{8}$$

Therefore, the pressure difference between neighboring channels is:

$$\Delta P_{U-rib}(x) = [(P_{inlet} - P(x)) - (P_{inlet} - P(x'))] = \frac{32 v_{A-CH} \mu_A}{d_h^2}[2nl_v + (2n-1)l_h - 2x] \tag{9}$$

where n is the parallel channel number.

$$\text{Accordingly}: \quad \begin{aligned} N_{A-DL}^{MeOH} &= -D_{A-DL,eff}^{MeOH} \frac{dC_{A-DL}^{MeOH}}{dy_{A-DL}} + \Gamma_A^2 C_{A-DL}^{MeOH} \\ \Gamma_A^2 &= \frac{32 v_{A-CH} k_{A-DL}^p}{l_h d_h^2}[2nl_v + (2n-1)l_h - 2x] \end{aligned} \tag{10}$$

Following mass conservation $dN_{A-DL}^{MeOH}/dy_{A-DL} = 0$, the distribution of methanol concentration across diffusion layer is given by

$$C_{A-DL}^{MeOH} = \frac{\left(C_{A-DL}^{MeOH}\big|_{y=0} - C_{A-DL}^{MeOH}\big|_{y=t_{A-DL}} \right)\exp((\Gamma_A^2/D_{A-DL,eff}^{MeOH})y_{A-DL}) + C_{A-DL}^{MeOH}\big|_{y=t_{A-DL}} - C_{A-DL}^{MeOH}\big|_{y=0}\exp((\Gamma_A^2/D_{A-DL,eff}^{MeOH})t_{A-DL})}{1 - \exp((\Gamma_A^2/D_{A-DL,eff}^{MeOH})t_{A-DL})} \tag{11}$$

The boundary conditions are $C_{A-DL}^{MeOH} = C_{A-DL}^{MeOH}\big|_{y=t_{A-DL}}$ at the anode catalyst layer and $C_{A-DL}^{MeOH} = C_{A-DL}^{MeOH}\big|_{y=0}$ at the interface between the anode channel and diffusion layer. The methanol mass flux at anode diffusion layer is then described as

$$N_{A-DL}^{MeOH} = \frac{\Gamma_A^2 C_{A-DL}^{MeOH}\big|_{y=t_{A-DL}} - \Gamma_A^2 C_{A-DL}^{MeOH}\big|_{y=0}\exp((\Gamma_A^2/D_{A-DL,eff}^{MeOH}t_{A-DL}))}{1 - \exp((\Gamma_A^2/D_{A-DL,eff}^{MeOH}t_{A-DL}))} = \frac{1}{6F}j_A + N_m^{MeOH} \tag{12}$$

which corresponds to the electricity generation as well as the methanol crossover through the PEM.

Hereafter, a first-order electrochemical reaction is adopted in the proposed model for both methanol oxidation and oxygen reduction hereafter. Consequently, Tafel kinetics of the first order are employed to describe the reaction current of methanol oxidation at the anode catalyst layer, namely:

$$\begin{aligned} j_A &= \Gamma_A^3 C_{A-DL}^{MeOH}\big|_{y=t_{A-DL}} \\ \Gamma_A^3 &= (j_{ref}^{MeOH}/C_{ref}^{MeOH})\exp((\alpha_A F/RT)\eta_A) \end{aligned} \tag{13}$$

Combining Eqs. (5) and (11), the equilibrium relation between methanol concentration at catalyst layer and channel|diffusion layer interface can be found, i.e.:

$$C_{A-DL}^{MeOH}\big|_{y=t_{A-DL}} = \Psi_{A-DL}^{w,U-rib} C_{A-DL}^{MeOH}\big|_{y=0} \tag{14}$$

where the equilibrium constant $\Psi_{A-DL}^{w,U-rib}$ is defined as

$$\Psi_{A-DL}^{w,U-rib} = \frac{\Gamma_A^2 \exp((\Gamma_A^2/D_{A-DL,eff}^{MeOH})t_{A-DL})/(1 - \exp((\Gamma_A^2/D_{A-DL,eff}^{MeOH})t_{A-DL}))}{(\Gamma_A^2/1 - \exp((\Gamma_A^2/D_{A-DL,eff}^{MeOH})t_{A-DL})) + (\Gamma_A^1 \exp((\Gamma_A^1/D_{m,eff}^{MeOH})t_m)/1 - \exp((\Gamma_A^1/D_{m,eff}^{MeOH})t_m)) - (\Gamma_A^3/6F)} \tag{15}$$

Due to the continuity of methanol flux at the anode, the flux in the diffusion layer can be described by effective mass-transfer at its interface toward the anode flow channel:

$$N_{A-DL}^{MeOH} = N_{A-CH-DL}^{MeOH} = h_{m,eff}^{MeOH}(C_{A-CH}^{MeOH} - C_{A-DL}^{MeOH}\big|_{y=0}) \tag{16}$$

where $h_{m,eff}^{MeOH}$ is the effective mass-transfer coefficient. As an approximation, the effective diffusion coefficient relating to a two-phase effect of fully developed laminar flow can be expressed as [18]

$$h_{m,eff}^{MeOH} = Sh \frac{D_{A-CH,eff}^{MeOH}}{t_{A-CH}} \tag{17}$$

As a result, the equilibrium relation between methanol concentration at the anode diffusion layer and its channel interface can then be derived by combining Eq. (12), Eq. (14), and Eq. (16):

$$C_{A-DL}^{MeOH}\big|_{y=0} = \Psi_{A-CH-DL}^{w,U-rib} C_{A-CH}^{MeOH} \tag{18}$$

where $\Psi_{A-CH-DL}^{w,U\text{-}rib}$ is an equilibrium constant under the assumption of instantaneous equilibrium at the interface, i.e.:

$$\Psi_{A-CH-DL}^{w,U\text{-}rib} = \frac{h_{m,eff}^{MeOH}}{\Gamma_A^2(\Psi_{A-DL}^{w,U\text{-}rib} - \exp((\Gamma_A^2/D_{A-DL,eff}^{MeOH})t_{A-DL})/1 - \exp((\Gamma_A^2/D_{A-DL,eff}^{MeOH})t_{A-DL})) + h_{m,eff}^{MeOH}} \tag{19}$$

According to mass conversation, the methanol flux from the channel to the diffusion layer can be described as

$$-t_{A-CH}v_{A-CH}\frac{dC_{A-CH}^{MeOH}}{dx} = N_{A-CH-DL}^{MeOH} = h_{m,eff}^{MeOH}(1 - \Psi_{A-CH-DL}^{w,U\text{-}rib})C_{A-CH}^{MeOH} \tag{20}$$

The concentration distribution of methanol along the anode channel $C_{A-CH}^{MeOH}(x)$ can be obtained by solving the differential equation Eq. (20). Subsequently, its distribution at the channel|diffusion layer interface $C_{A-DL}^{MeOH}\big|_{y=0}(x)$ and the anode catalyst layer $C_{A-DL}^{MeOH}\big|_{y=t_{A-DL}}(x)$ can be derived.

2.2.2. No under-rib mass transport region

Similar to that of the under-rib mass transport region, the mass flux of methanol is mainly driven by diffusion and the under-rib convection is neglected:

$$N_{A-DL}^{MeOH} = -D_{A-DL,eff}^{MeOH}\frac{dC_{A-DL}^{MeOH}}{dy_{A-DL}} \tag{21}$$

Based on mass conservation $dN_{A-DL}^{MeOH}/dy_{A-DL} = 0$, the methanol concentration is found linearly distributed in the diffusion layer:

$$C_{A-DL}^{MeOH} = \frac{\left(C_{A-DL}^{MeOH}\big|_{y=t_{A-DL}} - C_{A-DL}^{MeOH}\big|_{y=0}\right)}{t_{A-DL}}y_{A-DL} + C_{A-DL}^{MeOH}\big|_{y=0} \tag{22}$$

Similarly, the equilibrium relations of methanol concentration at different locations are given as

$$C_{A-DL}^{MeOH}\big|_{y=t_{A-DL}} = \Psi_{A-DL}^{w/o,U\text{-}rib}C_{A-DL}^{MeOH}\big|_{y=0}$$

$$C_{A-DL}^{MeOH}\big|_{y=0} = \Psi_{A-CH-DL}^{w/o,U\text{-}rib}C_{A-CH}^{MeOH} \tag{23}$$

where the equilibrium constants are

$$\Psi_{A-DL}^{w/o,U\text{-}rib} = \frac{-(D_{A-DL,eff}^{MeOH}/t_{A-DL})}{-(D_{A-DL,eff}^{MeOH}/t_{A-DL}) + \dfrac{\Gamma_A^1\exp((\Gamma_A^1/D_{m,eff}^{MeOH})t_m)}{1 - \exp((\Gamma_A^1/D_{m,eff}^{MeOH})t_m)} - \dfrac{\Gamma_A^2}{6F}} \tag{24}$$

$$\Psi_{A-CH-DL}^{w/o,U\text{-}rib} = \frac{h_{m,eff}^{MeOH}}{(1 - \Psi_{A-DL}^{w/o,U\text{-}rib})(D_{A-DL,eff}^{MeOH}/t_{A-DL}) + h_{m,eff}^{MeOH}}$$

As a consequence of mass conservation of methanol in the channel:

$$-t_{A-CH}v_{A-CH}\frac{dC_{A-CH}^{MeOH}}{dx} = h_{m,eff}^{MeOH}(1 - \Psi_{A-CH-DL}^{w/o,U\text{-}rib})C_{A-CH}^{MeOH} \tag{25}$$

As $\Psi_{A-CH-DL}^{w/o,U\text{-}rib}$ is not related to the methanol concentration in the channel C_{A-CH}^{MeOH}, the final solution for methanol distribution $C_{A-CH}^{MeOH}(x)$ in the channel is

$$C_{A-CH}^{MeOH}(x) = K\exp(\frac{-h_{m,eff}^{MeOH}(1 - \Psi_{A-CH-DL}^{w/o,U\text{-}rib})}{t_{A-CH}v_{A-CH}}x) \tag{26}$$

where K is the constant determined by the boundary conditions for the region without under-rib mass transport in the entire flow-filed. Subsequently, the distribution of methanol in the diffusion layer, $C_{A-DL}^{MeOH}\big|_{y=0}(x)$ and $C_{A-DL}^{MeOH}\big|_{y=t_{A-DL}}(x)$, can be derived.

The cell current density is calculated by integrating the local current density of Eq. (13):

$$I_{cell} = \int_0^{L_{total}} \Gamma_A^3 C_{A-DL}^{MeOH}\big|_{y=t_{A-DL}}(x)dx \tag{27}$$

where $C_{A-DL}^{MeOH}\big|_{y=t_{A-DL}}(x)$ is previously derived for regions with and under-rib mass transport.

The effective methanol diffusion coefficient $D_{A-DL,eff}^{MeOH}$ and the mass-transfer coefficient $h_{m,eff}^{MeOH}$ remain undetermined as these two parameters are affected by two-phase transport due to the existence of carbon dioxide.

2.3. Two-phase effect at anode

The diffusion layer used in a DMFC is normally made of carbon paper with a microfibrous structure and a pore size that ranges from a few to tens of microns. The paper is usually teflonized to impart a hydrophobic property. Together with carbon dioxide generation, liquid–gas

coexist in the capillaries of the layer. The two-phase transport in the diffusion layer is then governed primarily by capillary force due to the surface tension of the liquid–gas interfacial meniscus in the porous structure [37]. Therefore, the contact angle and liquid retention are important parameters in this region. The capillary pressure between the gas and liquid regions can be typically expressed as

$$P_c = P_g - P_l = \sigma \cos\theta \left(\frac{\varepsilon_A}{k_{A-DL}^p} \right)^{1/2} F(S) \tag{28}$$

where θ is surface contact angle, and the Leverett function $F(S)$ is the dimensionless capillary pressure as a function of the liquid saturation, S, which describes the ratio of liquid volume within the porous structure, namely:

$$F(S) = [1.417(1-S) - 2.120(1-S)^2 + 1.263(1-S)^3] \tag{29}$$

As the flow is assumed to be homogeneous, the liquid saturation S takes the average value of the entire flow region for the proposed model.

With back transfer of carbon dioxide through the diffusion layer to the anode channel, a localized thermodynamic equilibrium occurs in the liquid–gas region. Therefore, the gas phase at the anode diffusion layer also consists of saturated water and methanol vapor, i.e.:

$$P_g = P_{V,sat}^{H_2O} + P_{V,sat}^{MeOH} + P_g^{CO_2} \tag{30}$$

As a result, water and methanol are treated as a two-phase mixture. Hence, following two-phase mixture parameters will apply.

Density : $\rho = \rho_l S + \rho_g(1-S)$

Concentration : $C = C_l S + C_g(1-S)$ (31)

Diffusion-coefficient : $\rho D = \rho_l S D_l + \rho_g(1-S)D_g$

The effective diffusion coefficient for each phase of methanol can be expressed as

$$D_{A-DL,l}^{MeOH} = (\varepsilon_A S)^{\tau_A} D_l^{MeOH} \text{ and } D_{A-DL,g}^{MeOH} = [\varepsilon_A(1-S)]^{\tau_A} D_g^{MeOH} \tag{32}$$

The water saturation vapor pressure $P_{V,sat}^{H_2O}$ can be readily found from a steam table [38], whereas Henry's law is employed for the methanol vapor pressure [18].

$$P_{V,sat}^{MeOH} = k_H \chi_l^{MeOH} \tag{33}$$

where χ_l^{MeOH} is the liquid phase methanol molar fraction. For an average diluted solution, this fraction can be determined by the average liquid methanol concentration in the diffusion layer, i.e.:

$$\chi_l^{MeOH} = \frac{\overline{C_{A-DL,l}^{MeOH}}}{\overline{C_{A-DL,l}^{H_2O}} + \overline{C_{A-DL,l}^{MeOH}}} \underset{\overline{C_{A-DL,l}^{H_2O}} \gg \overline{C_{A-DL,l}^{MeOH}}}{\approx} \frac{\overline{C_{A-DL,l}^{MeOH}}}{\overline{C_{A-DL,l}^{H_2O}}} = \frac{M_l^{H_2O} \overline{C_{A-DL,l}^{MeOH}}}{\rho_l^{H_2O}} \tag{34}$$

By applying the ideal gas law as well as the two-phase mixture parameter definition, the methanol vapor pressure can be related to the average methanol concentration, as follows:

$$P_{V,sat}^{MeOH} = \frac{k_H \cdot M_l^{H_2O}/\rho_l^{H_2O}}{S + [k_H M_l^{H_2O}(1-S)/(\rho_l^{H_2O}RT)]} \overline{C_{A-DL}^{MeOH}} \tag{35}$$

The carbon dioxide is assumed to be non-soluble in liquid to make the model simpler. Therefore, its partial pressure can be related to the average concentration $\overline{C_{A-DL}^{CO_2}}$ in diffusion layer by employing ideal gas law, $P_g^{CO_2} = RT\overline{C_{A-DL}^{CO_2}}$.

In the channel region, two-phase transport is rather simple as a homogeneous bubble flow is assumed. The gas phase carbon dioxide is saturated with water and methanol vapor. The total pressure of the gas phase species is equal to that of liquid due to an assumption of homogeneous steady flow. Similarly, the partial pressure of each species is proportioned to its average concentration in the anode channel, i.e., $\overline{C_{A-CH}^{MeOH}}$ and $\overline{C_{A-CH}^{CO_2}}$ respectively. Assuming α is a void fraction which represents the gas volume ratio in the channel, the effective diffusion coefficient of gas and liquid phase methanol in the channel can be described as

$$D_{A-CH,l,eff}^{MeOH} = \frac{(1-\alpha)}{\tau_A} D_l^{MeOH} \text{ and } D_{A-CH,g,eff}^{MeOH} = \frac{\alpha}{\tau_A} D_g^{MeOH} \tag{36}$$

Consequently, the two-phase effective diffusion coefficient in the mass-transfer coefficient $h_{m,eff}^{MeOH}$, as shown in Eq. (17), is properly described.

As a result, two pressure equilibrium statements at the anode channel and the diffusion layer are set up with undetermined two-phase parameters, S and α. The solution can be found from knowledge of the average concentration distribution of each species, namely $\overline{C_{A-DL}^{MeOH}}$ and $\overline{C_{A-DL}^{CO_2}}$ for the diffusion layer, and $\overline{C_{A-CH}^{MeOH}}$ and $\overline{C_{A-CH}^{CO_2}}$ for the anode channel. The concentration distribution of methanol can be easily calculated from the equations derived above by their integration over the entire region. The derivation of the concentration distribution for carbon dioxide will be presented in the following section.

2.4. Carbon dioxide mass transport at anode

Carbon dioxide is a product of the fuel cell reaction. Since the PEM is assumed to be impermeable to the gas, there is no internal leaking flux of carbon dioxide. Therefore, the mass flux of carbon dioxide travels from the catalyst layer to the anode channel through the diffusion

layer and is related only to the methanol flux, as in Eqs. (14) and (23), for regions with or without under-rib convection, namely:

$$N_{A-CH-DL}^{CO_2} = N_{A-DL}^{CO_2} = \frac{1}{6F}j_A = \frac{1}{6F}\Gamma_A^3 C_{A-DL}^{MeOH}\Big|_{y=t_{A-DL}}(x) \tag{37}$$

Accordingly, the carbon dioxide concentration in the anode channel $C_{A-CH}^{CO_2}(x)$ can be found from the mass conservation:

$$t_{A-CH}v_{A-CH}\frac{dC_{A-CH}^{CO_2}}{dx} = \frac{1}{6F}\Gamma_A^3 C_{A-DL}^{MeOH}\Big|_{y=t_{A-DL}}(x) \tag{38}$$

The carbon dioxide concentration at the interface between the channel and the diffusion layer $C_{A-DL}^{CO_2}\big|_{y=0}(x)$ is then determined by mass-transfer transport:

$$h_{m,eff}^{CO_2}\left(C_{A-DL}^{CO_2}\Big|_{y=0} - C_{A-CH}^{CO_2}\right) = \frac{1}{6F}\Gamma_A^3 C_{A-DL}^{MeOH}\Big|_{y=t_{A-DL}}(x) \tag{39}$$

while the concentration in the channel/diffusion layer can be derived as in previous process for methanol derivation in regions with or without under-rib mass transport.

2.4.1. Under-rib mass transport region

The constant carbon dioxide flux is driven by a concentration gradient as well as a pressure difference between neighboring channels, but in the reverse direction to the methanol flux, i.e.:

$$N_{A-DL}^{CO_2} = D_{A-DL,eff}^{CO_2}\frac{dC_{A-DL}^{CO_2}}{dy_{A-DL}} + \Gamma_A^2 C_{A-DL}^{CO_2} \tag{40}$$

where the effective porosity is used to calculate the effective diffusion coefficient of carbon dioxide, $D_{A-DL,eff}^{CO_2} = [(1-S)\varepsilon_C]^{\tau_C}D_g^{CO_2}$. The carbon dioxide distribution in the diffusion layer can be derived as

$$C_{A-DL}^{CO_2} = \frac{\left(C_{A-DL}^{CO_2}\big|_{y=0} - C_{A-DL}^{CO_2}\big|_{y=t_{A-DL}}\right)\exp\left((-\Gamma_A^2/D_{A-DL,eff}^{CO_2})y_{A-DL}\right) + C_{A-DL}^{CO_2}\big|_{y=t_{A-DL}} - C_{A-DL}^{CO_2}\big|_{y=0}\exp\left((-\Gamma_A^2/D_{A-DL,eff}^{CO_2})t_{A-DL}\right)}{1 - \exp\left((\Gamma_A^2/-D_{A-DL,eff}^{CO_2})t_{A-DL}\right)} \tag{41}$$

The carbon dioxide flux is then given by

$$N_{A-DL}^{CO_2} = \frac{\Gamma_A^2 C_{A-DL}^{CO_2}\big|_{y=t_{A-DL}} - \Gamma_A^2 C_{A-DL}^{CO_2}\big|_{y=0}\exp\left((-\Gamma_A^2/D_{A-DL,eff}^{CO_2})t_{A-DL}\right)}{1 - \exp\left((-\Gamma_A^2/D_{A-DL,eff}^{CO_2})t_{A-DL}\right)} \tag{42}$$

2.4.2. No under-rib mass transport region

If under-rib convection is considered, the carbon dioxide flux will be treated as a diffusion flow linearly distributed across the diffusion layer, i.e.:

$$N_{A-DL}^{CO_2} = D_{A-DL,eff}^{CO_2}\frac{dC_{A-DL}^{CO_2}}{dy_{A-DL}} = D_{A-DL,eff}^{CO_2}\frac{C_{A-DL}^{CO_2}\big|_{y=t_{A-DL}} - C_{A-DL}^{CO_2}\big|_{y=0}}{t_{A-DL}} \tag{43}$$

and,

$$C_{A-DL}^{CO_2} = \frac{\left(C_{A-DL}^{CO_2}\big|_{y=t_{A-DL}} - C_{A-DL}^{CO_2}\big|_{y=0}\right)}{t_{A-DL}}y_{A-DL} + C_{A-DL}^{CO_2}\big|_{y=0} \tag{44}$$

Consequently, the average concentrations carbon dioxide in the anode diffusion layer $\overline{C_{A-DL}^{CO_2}}$ and the channel $\overline{C_{A-CH}^{CO_2}}$ are now available for the two-phase model.

2.5. Oxygen mass transport at cathode

The situation at the cathode is more simple without the two-phase effect. The mass balance of oxygen at the cathode side is similar to that of methanol at the anode with the corresponding parameters in their gas phase value. The oxygen supplied at the cathode catalyst site combines with electrons to provide electricity generation, and also partially reacts with crossovered methanol and thereby reduces the mixed potential of the cathode. Thus

$$N_{C-CH-DL}^{O_2} = N_{C-DL}^{O_2} = \frac{1}{4F}j_C + \frac{3}{2}N_m^{MeOH} \tag{45}$$

where,

$$j_C = \Gamma_C^2 C_{C-DL}^{O_2}\Big|_{y=t_{C-DL}}$$
$$\Gamma_C^2 = (j_{ref}^{O_2}/C_{ref}^{O_2})\exp\left((\alpha_C F/RT)\eta_C\right) \tag{46}$$

2.5.1. Under-rib mass transport region

Oxygen flux is driven by a concentration gradient and a pressure drop between adjacent channels:

$$N_{C-DL}^{O_2} = -D_{C-DL,eff}^{O_2} \frac{dC_{C-DL}^{O_2}}{dy_{C-DL}} + \Gamma_C^1 C_{C-DL}^{O_2}$$

$$\Gamma_C^1 = \frac{32\nu_{C-CH} k_{C-DL}^p}{l_h d_h^2} [2n l_\nu + (2n-1)l_h - 2x]$$

(47)

where the effective diffusion coefficient is $D_{C-DL,eff}^{O_2} = (\varepsilon_C)^{\tau_C} D_{C-DL}^{O_2}$.

Following the same derivation of anode methanol distribution, the oxygen distribution in the cathode diffusion layer and its concentration at the catalyst layer can be expressed as

$$C_{C-DL}^{O_2} = \frac{(C_{C-DL}^{O_2}|_{y=0} - C_{C-DL}^{O_2}|_{y=t_{C-DL}})\exp((\Gamma_C^1/D_{C-DL,eff}^{O_2})y_{C-DL}) + C_{C-DL}^{O_2}|_{y=t_{C-DL}} - C_{C-DL}^{O_2}|_{y=0}\exp((\Gamma_C^1/D_{C-DL,eff}^{O_2})t_{C-DL})}{1 - \exp((\Gamma_C^1/D_{C-DL,eff}^{O_2})t_{C-DL})} C_{C-DL}^{O_2}|_{y=t_{C-DL}}$$

$$= \Psi_{C-DL}^{w,U-rib} C_{C-DL}^{O_2}|_{y=0} + \Psi' N_m^{MeOH}$$

(48)

where the equilibrium constants are

$$\Psi_{C-DL}^{w,U-rib} = \frac{\Gamma_C^1 \exp((\Gamma_C^1/D_{C-DL,eff}^{O_2})t_{C-DL})}{\dfrac{\Gamma_C^1}{1 - \exp((\Gamma_C^1/D_{C-DL,eff}^{O_2})t_{C-DL})} - \dfrac{\Gamma_C^2}{4F}}$$

$$\Psi' = \frac{3/2}{\dfrac{\Gamma_C^1}{1 - \exp((\Gamma_C^1/D_{C-DL,eff}^{O_2})t_{C-DL})} - \dfrac{\Gamma_C^2}{4F}}$$

(49)

The carbon dioxide concentration at the interface between the channel and the diffusion layer can be derived from mass-transfer, $N_{C-CH-DL}^{O_2} = h_{m,eff}^{O_2}(C_{C-CH}^{O_2} - C_{C-DL}^{O_2}|_{y=0})$,

$$C_{C-DL}^{O_2}|_{y=0} = \Psi_{C-CH-DL}^{w,U-rib} C_{C-CH}^{O_2} + \Psi' N_m^{MeOH}$$

(50)

where the equilibrium constants are

$$\Psi_{C-CH-DL}^{w,U-rib} = \frac{h_{m,eff}^{O_2}}{\Gamma_C^1[\Psi_{C-DL}^{w,U-rib} - \exp((\Gamma_C^1/D_{C-DL,eff}^{O_2})t_{C-DL})]/[1 - \exp((\Gamma_C^1/D_{C-DL,eff}^{O_2})t_{C-DL})] + h_{m,eff}^{O_2}}$$

$$\Psi' = \frac{\Gamma_C^1 \Psi'/[1 - \exp((\Gamma_C^1/D_{C-DL,eff}^{O_2})t_{C-DL})]}{\Gamma_C^1[\Psi_{C-DL}^{w,U-rib} - \exp((\Gamma_C^1/D_{C-DL,eff}^{O_2})t_{C-DL})]/[1 - \exp((\Gamma_C^1/D_{C-DL,eff}^{O_2})t_{C-DL})] + h_{m,eff}^{O_2}}$$

(51)

Finally, the oxygen concentration along the channel $C_{C-CH}^{O_2}(x)$ are derived by considering mass conservation and distribution in the diffusion layer, i.e.:

$$-t_{C-CH}\nu_{C-CH} \frac{dC_{C-CH}^{O_2}}{dx} = h_{m,eff}^{O_2}(1 - \Psi_{C-CH-DL}^{w,U-rib})C_{C-CH}^{O_2} - h_{m,eff}^{O_2} \Psi' N_m^{MeOH}$$

(52)

2.5.2. No under-rib mass transport region

Darcy-type convection flux is neglected in the oxygen flux. Therefore, the oxygen concentration is found to be linearly distributed along the diffusion layer, i.e.:

$$N_{C-DL}^{O_2} = -D_{C-DL,eff}^{O_2} \frac{dC_{C-DL}^{O_2}}{dy_{C-DL}} = -D_{C-DL,eff}^{O_2} \frac{(C_{C-DL}^{O_2}|_{y=t_{C-DL}} - C_{C-DL}^{O_2}|_{y=0})}{t_{C-DL}}$$

(53)

Consequently,

$$C_{C-DL}^{O_2} = \frac{(C_{C-DL}^{O_2}|_{y=t_{C-DL}} - C_{C-DL}^{O_2}|_{y=0})}{t_{C-DL}} \cdot y_{C-DL} + C_{C-DL}^{O_2}|_{y=0}$$

$$C_{C-DL}^{O_2}|_{y=t_{C-DL}} = \Psi_{C-DL}^{w/o,U-rib} \cdot C_{C-DL}^{O_2}|_{y=0} - \Psi' \cdot N_m^{MeOH}$$

$$C_{C-DL}^{O_2}|_{y=0} = \Psi_{C-CH-DL}^{w/o,U-rib} \cdot C_{C-CH}^{O_2} + \Psi' \cdot N_m^{MeOH}$$

(54)

Table 1
Physicochemical properties.

Parameters	Symbol	Value
Anode inlet pressure (Pa)	$P_{A,in}$	1.01325×10^5
Cathode inlet pressure (Pa)	$P_{C,in}$	1.01325×10^5
Oxygen input concentration at cathode (mol cm^{-3})	C_{in}^C	0.21×10^{-6} ($P_{C,in}/RT$)
Permeability of PEM (cm^2)	k_m^P	1.17×10^{19} exp$(-19098/T)$
Permeability of anode diffusion layer (cm^2) [31]	k_{A-DL}^P	1×19^{-9}
Permeability of anode diffusion layer (cm^2) [31]	k_{C-DL}^P	1×19^{-9}
Electro-osmosis drag of water (cm^3 mol^{-1}) [35]	$n_{EOD}^{H_2O}$	2.5
Electro-osmosis drag of methanol (cm^3 mol^{-1}) [35]	χ_{EOD}^{MeOH}	45
Viscosity of liquid water (Pa s) [39]	μ_A	$0.458509 - 5.30474 \times 10^{-3}T + 2.31231 \times 10^{-5}T^2 - 4.49161 \times 10^{-8}T^3 + 3.27681 \times 10^{-11}T^4$
Viscosity of gas (Pa s) [39]	μ_C	2.03×10^{-5}
Diffusion coefficient of liquid methanol (cm^2 s^{-1}) [40]	D_l^{MeOH}	$(10(-5.4163 - (999.778/T))) \times 10^4$
Diffusion coefficient of gas methanol (cm^2 s^{-1}) [40]	D_g^{MeOH}	$-6.954 \times 10^{-2} + 4.5986 \times 10^{-4}T + 9.4979 \times 10^{-7}T^2$
Diffusion coefficient of carbon dioxide (cm^2 s^{-1}) [18]	$D_g^{CO_2}$	0.3
Diffusion coefficient of oxygen (cm^2 s^{-1}) [41]	$D_g^{O_2}$	$1.77(T/273)^{1.823}(10.13/P_{C,in})$
Porosity of PEM	ε_m	0.3
Porosity of anode diffusion layer	ε_A	0.6
Porosity of cathode diffusion layer	ε_c	0.7
Tortuosity of PEM	τ_m	1.8
Tortuosity of anode diffusion layer	τ_A	1.5
Tortuosity of cathode diffusion layer	τ_C	1.5
Proton conductivity of PEM (S cm^{-1}) [42]	κ_m	0.123
Reference anode exchange current density (A cm^{-3}) [18]	j_{ref}^{MeOH}	9.425×10^{-3} exp$((35570)/R((1/353)-(1/T)))$
Reference cathode exchange current density (A cm^{-3}) [18]	$j_{ref}^{O_2}$	4.222×10^{-6} exp$((73200/R)((1/353)-(1/T)))$
Reference concentration of methanol (mol cm^{-3})	C_{ref}^{MeOH}	0.001
Reference concentration of oxygen (mol cm^{-3})	$C_{ref}^{O_2}$	0.002
Anodic transfer coefficient	α_A	0.54
Cathodic transfer coefficient	α_C	0.76
Sherwood number [18]	Sh	2.693
Interfacial tension (S cm^{-1}) [37]	σ	6.25
Contact angle (°)	θ	110
Contact resistance (Ω cm^2)	$R_{contact}$	0.01

where the equilibrium constants are

$$\Psi_{C-DL}^{w/o,U-rib} = \frac{D_{C-DL,eff}^{O_2}/t_{C-DL}}{D_{C-DL,eff}^{O_2}/t_{C-DL} + (\Gamma_C^2/4 \cdot F)} \text{ and } \Psi_{C-DL}^{'w/o,U-rib} = \frac{3/2}{D_{C-DL,eff}^{O_2}/t_{C-DL} + (\Gamma_C^2/4 \cdot F)} \tag{55}$$

$$\Psi_{C-CH-DL}^{w/o,U-rib} = \frac{h_{m,eff}^{O_2}}{(1/4F)\Gamma_C^2 \Psi_{C-DL}^{w/0,U-rib} + h_{m,eff}^{O_2}} \text{ and } \Psi_{C-CH-DL}^{w/o,U-rib} = \frac{(1/4F)\Gamma_C^2 \Psi_{C-DL}^{w/0,U-rib} - (3/2)}{(1/4F)\Gamma_C^2 \Psi_{C-DL}^{w/0,U-rib} + h_{m,eff}^{O_2}} \tag{56}$$

Similarly, the oxygen concentration in the cathode channel and its distribution in the diffusion layer can then be determined, namely:

$$-t_{C-CH}v_{C-CH}\frac{dC_{C-CH}^{O_2}}{dx} = h_{m,eff}^{O_2}(1 - \Psi_{C-CH-DL}^{w/o,U-rib})C_{C-CH}^{O_2} - h_{m,eff}^{O_2}\Psi' N_m^{MeOH} \tag{57}$$

The cell current density is then calculated by integration of the local current density at cathode.

$$I_{cell} = \int_0^{L_{total}} \Gamma_C^2 C_{C-DL}^{O_2}(x)dx \tag{58}$$

2.6. Cell voltage

Once the current density and the overpotentials of the anode and the cathode are obtained, the cell voltage can be determined by subtracting the activation losses at the two electrodes, as well as the ohmic contact potential and PEM potential from the thermodynamic
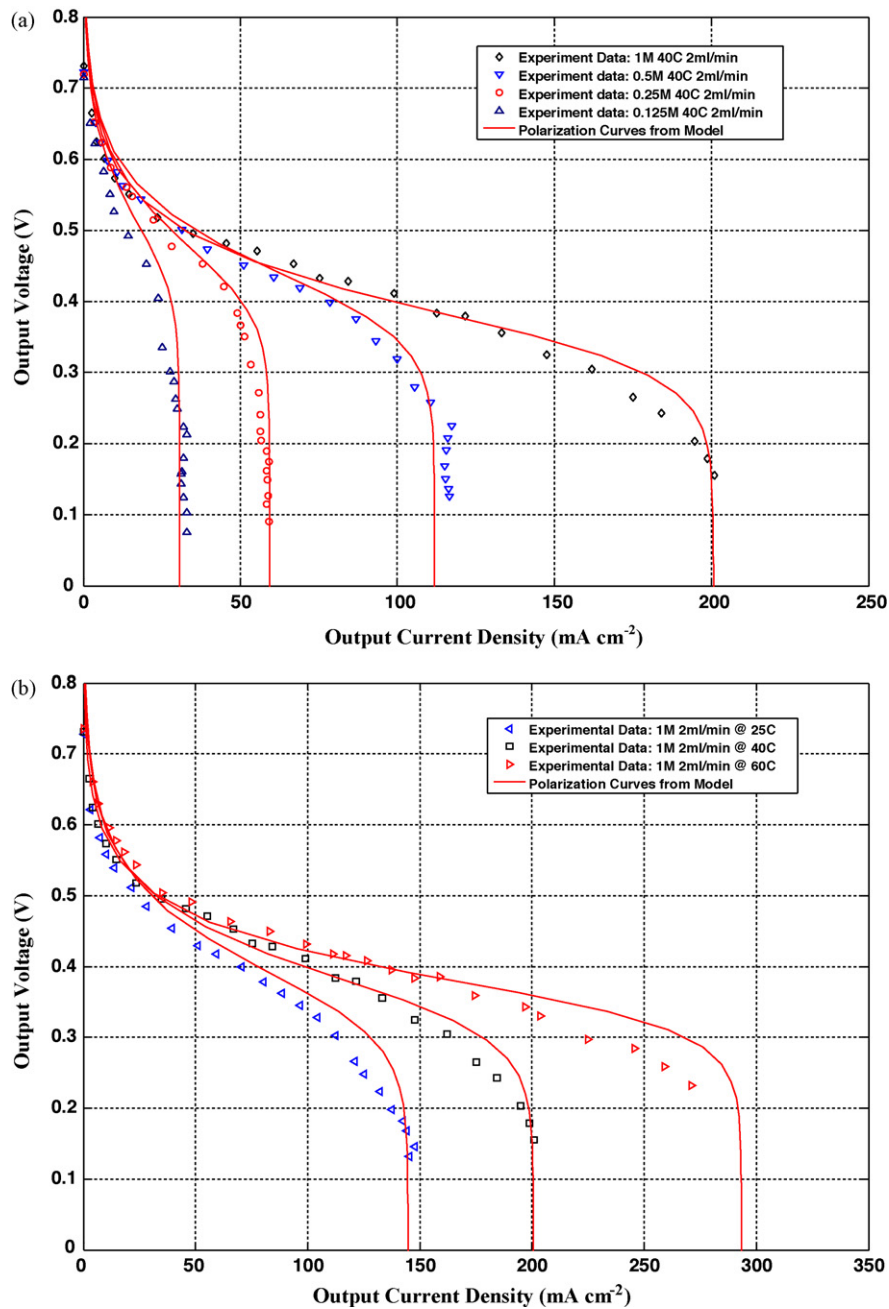
Fig. 2. Validation of present model against experimental data for a 5 cm² single-cell DMFC: (a) feeding with different concentration methanol solutions, 0.125, 0.25, 0.5, and 1 M; (b) under different operating temperatures, 25, 40 and 60 °C, with 1 M feeding methanol solution. Flow rate of methanol in anode channel is 2 ml min⁻¹. Air is supplied at cathode with flow rate of 300 ml min⁻¹ in all cases.

equilibrium potential. Hence

$$V_{cell} = V_0^{O_2} - V_0^{MeOH} - \eta_A - \eta_C - I_{cell}\frac{t_m}{\kappa_m} - I_{cell}R_{contact} \tag{59}$$

where $V_0^{O_2}$ and V_0^{MeOH} are the thermodynamic equilibrium potentials of oxygen reduction and methanol oxidation, their difference is set as 1.21 V for the theoretical thermodynamic cell voltage adopted in this study.

3. Experimental setup

3.1. DMFC

A single-cell DMFC that consisted of a membrane electrode assembly (MEA) sandwiched between two graphite blocks (POCO Graphite Inc., Decatur, TX) was used for performance measurement. The active area of the MEA was 5 cm² and a Nafion® 117 membrane was employed. The anode catalyst loading on the membrane was 4 mg cm⁻² of Pt–Ru black with an atomic ratio of 1:1. At the cathode side, only Pt was applied with the same loading of 4 mg cm⁻². Before assembly into a single-cell, the MEA was pretreated to improve its water
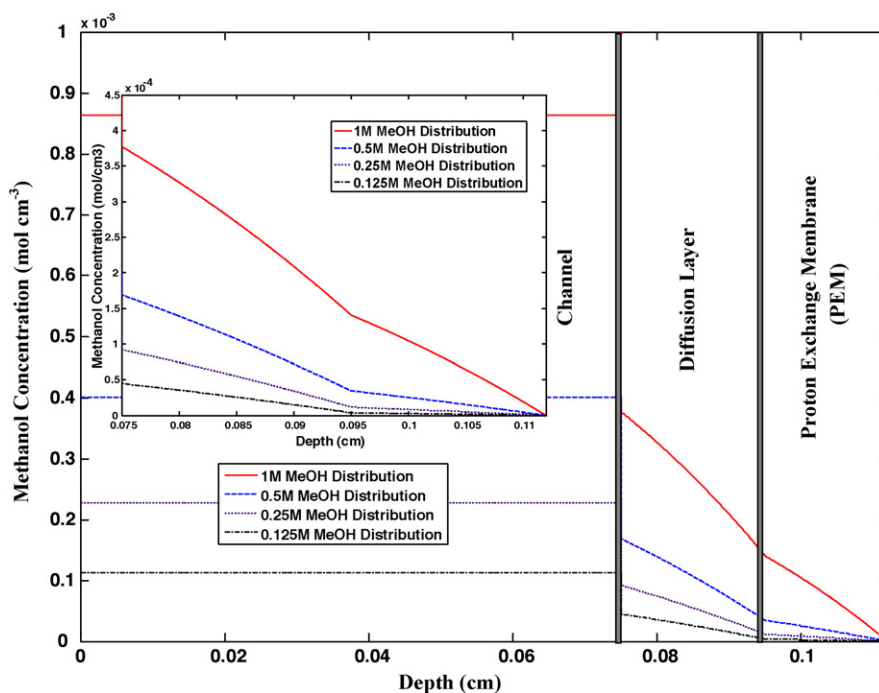
Fig. 3. Modelling results of methanol concentration distribution within anode channel, diffusion layer and PEM for different input methanol concentrations, 0.125, 0.25, 0.5, and 1 M, at V_{cell} = 0.35 V and 40 °C, 2 ml min^{-1} for MeOH, 300 ml min^{-1} for air.

content by rinsing in 50 °C deionized (DI) water for 5 h and then storing overnight in DI water at room temperature. The flow-fields for fuel transport and distribution were fabricated from graphite blocks with a SSC pattern. The channel had a square-shaped cross-section. The entire flow-field consisted of 14 parallel channels. The dimensions of each part in the flow-field are described in Fig. 1. With two polytetrafluoroethylene (PTFE) coated fiberglass gaskets, the flow-field plates were fastened to the MEA, with carbon cloth (E-TEK B-1, Type A) and E-TEK ELAT® (LT1400-W) as the diffusion layers at the anode and cathode respectively. The current-collectors on both sides were gold plated to reduce electrical resistance.

3.2. Measurement conditions

After assembly, the DMFC hardware was placed in a temperature-controlled chamber (ETAC, HISPEC HT210) for performance measurements. The temperature was monitored with a thermometer (FLUKE 179) attached to the flow-field plates. At the anode side, the aqueous methanol solution was supplied by a digital peristaltic pump (Longer, LEAD-1) with an adjustable flow rate. At the same time, the oxygen was supplied by a diaphragm air-pump (HAILEA, AC0-9610) from the ambient environment. An electronic load (Chroma 63106) was employed to record the current–voltage (I–V) curves. Before each measurement, the DMFC was first operated under a high cell voltage output (0.5 V) and a high current output (0.9 A) at 60 °C for 5 h to activate fully the MEA.

4. Results and discussion

4.1. Model validation

The experimental data for model validation was collected with the above setup under different operating conditions, i.e., variable methanol concentrations (0.125, 0.25, 0.5, and 1 M) and operating temperatures (25, 40, and 60). The flow rate of methanol is set at 2 ml min^{-1}, and air flow rate is 300 ml min^{-1}. The physical parameters used in the proposed model are tabulated in Table 1. In Fig. 2a, the modelling results of the cell I–V curves at different methanol concentrations and 40 °C operating temperature are verified and compared with experimental data. The results show a reasonable agreement between the two sets of data. The same is also observed in Fig. 2b for DMFC performance at different operating temperatures with 1 M methanol solution. Thus, the mathematical model developed in this study is believed to be realistic for DMFC performance analysis and prediction.

For various methanol concentrations at 40 °C and a cell output voltage of 0.35 V, the corresponding average methanol concentration within the channel, diffusion layer and PEM are profiled in Fig. 3. The distribution of the methanol concentration across the anode diffusion layer and PEM are also depicted in the expanded figure. The non-linear methanol distribution in the diffusion layer implies that under-rib mass transport improves mass transport in this layer. The relatively low methanol concentration in the catalyst layer indicates that the electrochemical reaction at the anode is still restricted by methanol transport, even though excess methanol is supplied in the anode channel. In all regions, the diffusion layer plays a major role in the total mass-transfer resistance. Higher methanol concentration at the input enhances mass transport. On the other hand, it also induces higher methanol crossover flux in the PEM, as seen in Fig. 3. The limiting mass-transport phenomenon occurs earlier with lower methanol concentration at the input, as indicated in Fig. 4. The methanol concentration in the catalyst layer is nearly zero with 0.125 M of input concentration. Consequently, the crossover flux in the PEM is much lower since most of the methanol is consumed for the electricity generating reaction on the catalyst.
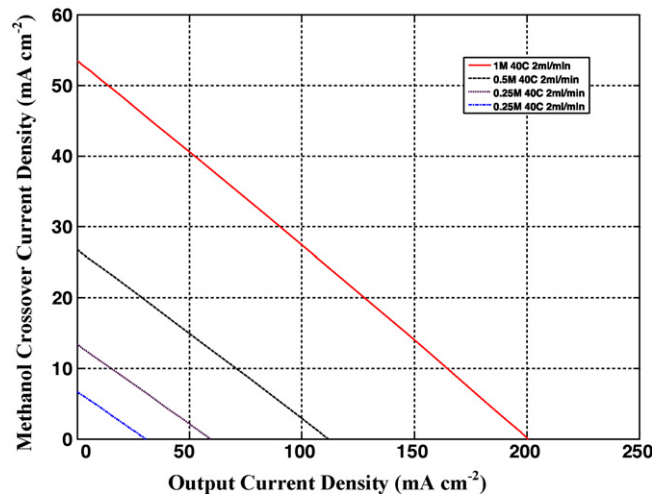
Fig. 4. Leaking current density caused by methanol crossover for different input methanol concentrations, 0.125, 0.25, 0.5, and 1 M, with 2 ml min^{-1} flow rate at 40 °C.

4.2. Analysis of methanol crossover

Methanol crossover is driven by diffusion, electro-osmosis and convection. These three factors contribute differently under different operating conditions. Nevertheless, all three depend on the local methanol concentration in the PEM. Hence, the maximum crossover flux is expected at the open-circuit voltage where the highest mass-transfer of un-reacted methanol occurs. When the current density increases, the excess methanol at the interface between the anode catalyst layer and the PEM decreases. Accordingly, methanol crossover reduces to almost zero after the current density approaches its limiting point where nearly all methanol is consumed by the electrochemical reaction. This is depicted in Fig. 4 by converting the methanol crossover flux into the induced leakage current density, i.e.:

$$I_{leak} = 6FN_m^{MeOH} \tag{60}$$

The high leakage current density, which occurs in the low output current density region, brings more severe voltage reduction, as shown in Fig. 2a. The two partial fluxes, namely, diffuse and electro-osmosis drag, in methanol crossover have been investigated and are shown in Fig. 5 for 0.5 and 1 M input methanol densities, respectively. Due to the lack of a significant pressure difference between the anode and the cathode, the convection contribution is neglected. The result indicates that diffusion mainly dominates in methanol crossover except in the region near the limiting current density. In this region, the methanol concentration at the interface of the catalyst layer and the PEM decreases due to the mass transport limitation and high current output. Therefore, the diffuse methanol flux governed by the concentration gradient in the PEM is markedly suppressed. The electro-osmosis drag flux, on the other hand, does not decrease significantly because it is proportional not only to the decrease in methanol concentration but also to the increase in cell current density. Once the current density reaches its limiting point, the diffuse flux becomes zero since there is no concentration gradient. The electro-osmosis drag flux of methanol also reduces to zero because there is no methanol content in the electro-osmosis water flux transferring through the PEM.

The temperature effect on the methanol concentration induced crossover is presented in Fig. 6. Methanol crossover gives us to a voltage reduction at low cell current density. The phenomenon is enhanced by raising the operating temperature from 40 to 60 °C. It is thought that temperature-enhanced methanol transport brings a relatively higher methanol concentration at the interface between the catalyst layer
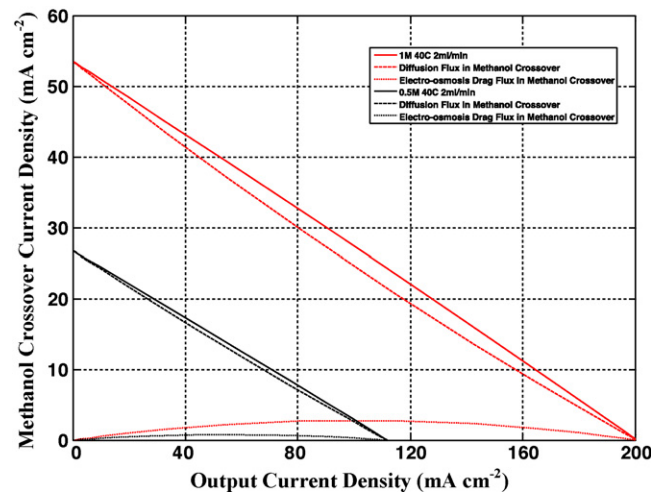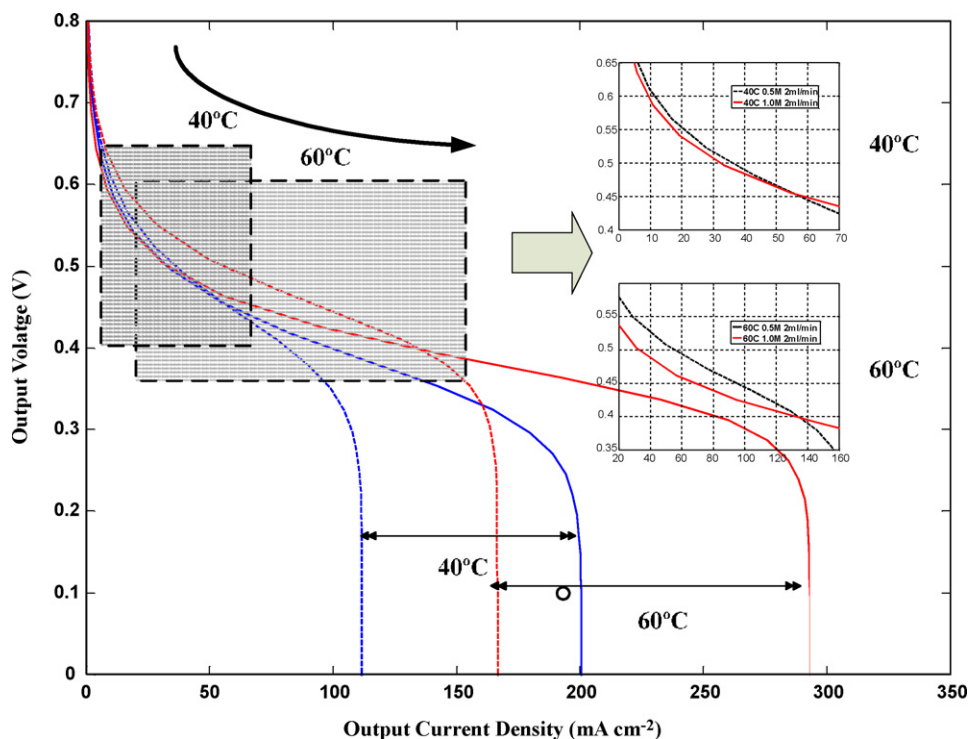

Fig. 5. Comparison between diffusion and electro-osmosis drag partial flux in methanol crossover flux for 0.5 and 1 M input methanol concentrations, with 2 ml min^{-1} flow rate at 40 °C.

Fig. 6. Cell voltage loss caused by methanol crossover in low current density regions with methanol concentration increase (0.5–1 M) with 2 ml min^{-1} flow rate under different operating temperatures, (40 and 60 °C).

and PEM. At higher operating temperatures, a higher diffusion coefficient applies to both liquid and gas phase methanol. At the same time, the saturated methanol concentration in the gas phase also increases to give fast methanol transport.

4.3. Effects of two-phase and under-rib mass transport

To investigate the two-phase mass transport effect on cell performance, the *I–V* curve for 1 M input methanol at 40 °C was simulated. The liquid saturation S is assumed to be unity and thereby represents only liquid phase transport at the anode. The result is shown in Fig. 7 for the case of an under-rib mass transport effect. The limiting current density is 147.0 mA cm^{-2} which is much smaller than that for two-phase mass transport, viz., 200.6 mA cm^{-2}. Thus reveals that methanol transport in the gas phase is important for a sufficient fuel supply to the reaction sites. Moreover, the cell voltage reduction induced by methanol crossover is noted at a low current density where the liquid phase transport situation gives a higher cell output voltage compared with that for two-phase transport. The phenomenon is attributed to enhanced methanol transport in the gas phase that in more severe methanol crossover. Accordingly, the theoretical limiting current density can be calculated by setting the methanol concentration to zero at the interface between the anode catalyst layer and the
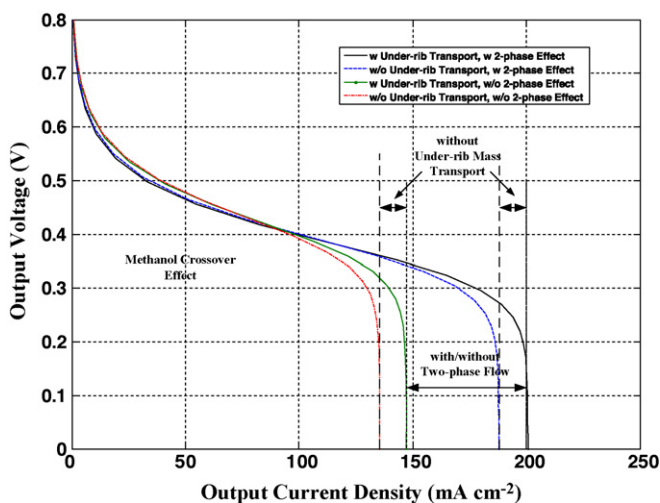
Fig. 7. Influence of two-phase flow phenomenon on DMFC performance, with and without under-rib mass transport consideration effects, 1 M input methanol solution with 2 ml min^{-1} flow rate at 40 °C operating temperature.

PEM, i.e.:

$$I_{\lim} = \frac{6F}{(1/h_m^{MeOH}) + (1/\Gamma_A^2)[1 - (1/\exp((\Gamma_A^2/D_{A-DL}^{MeOH})t_{A-DL}))]} C_{A-CH}^{MeOH} \qquad (61)$$

With an input methanol concentration of 1 M, the calculated limiting current density is 153.7 mA cm^{-2}, which is consistent with the modelling result given in Fig. 7.

By further ignoring the under-rib mass transport effect, the above equation can be simplified as

$$I_{\lim} = \frac{6F}{(1/h_m^{MeOH}) + (t_{A-DL}/D_{A-DL}^{MeOH})} C_{A-CH}^{MeOH} \qquad (62)$$

Consequently, the limiting current density has a relatively smaller value of 135.5 mA cm^{-2} with both effects ignored, which is also reasonably close to the modelling result of 138.4 mA cm^{-2}. The difference with and without under-rib mass transport effect, implies that the facilitated methanol transport toward the catalyst layer is influenced by under-rib mass transport. The significance of under-rib mass transport on performance is however, less than that caused by the two-phase effect. Performance data with the under-rib mass transport effect subtracted from the two-phase mass transport are presented in Fig. 7.
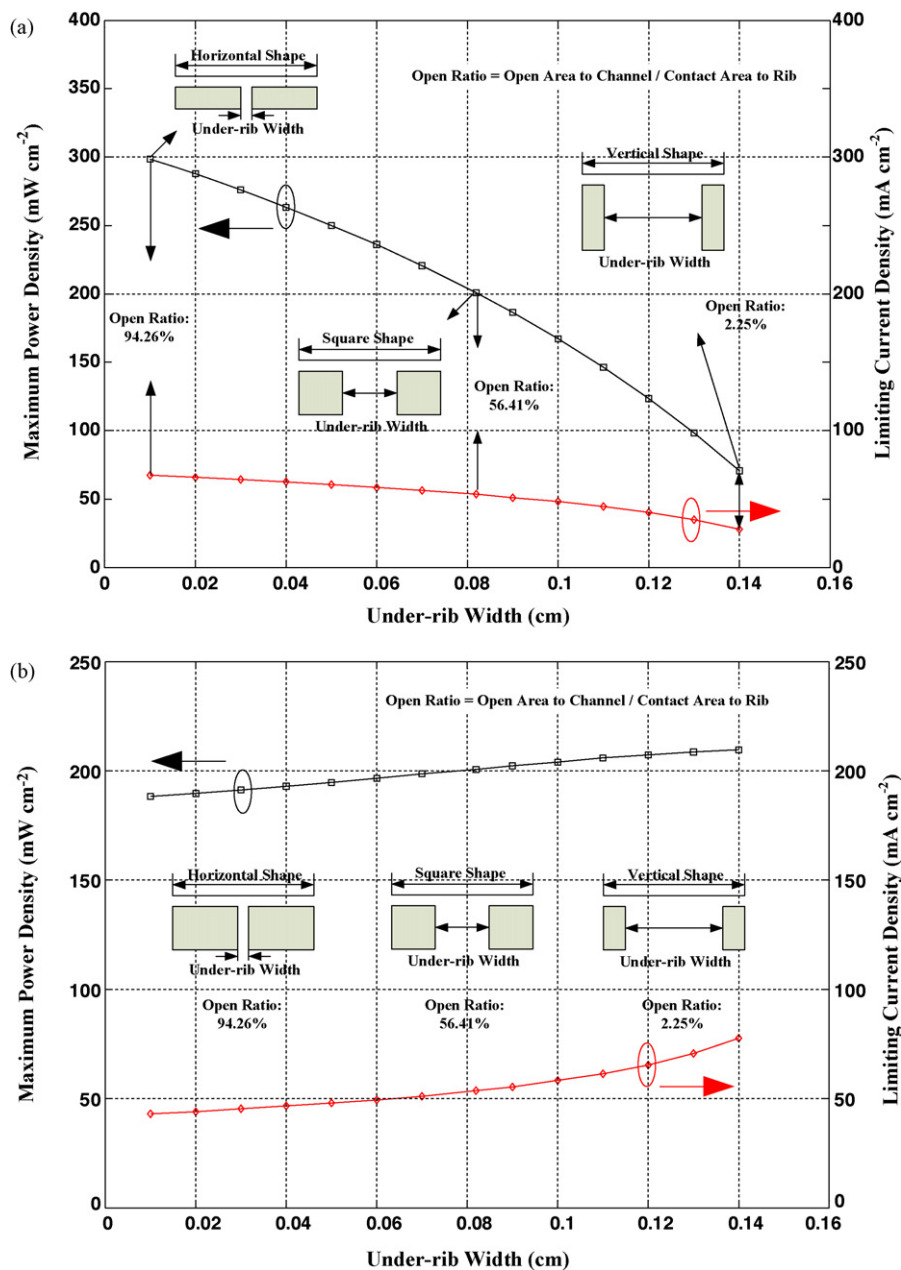
Fig. 8. Flow-field structure and channel cross-section effects on DMFC limiting current density and maximum power output: (a) under-rib width increases with same cross-section area; (b) under-rib width increases with same channel depth. Entire flow-field area and total parallel channel number unchanged in both cases. 1 M input methanol solution with 2 ml min^{-1} flow rate at 40 °C operating temperature.
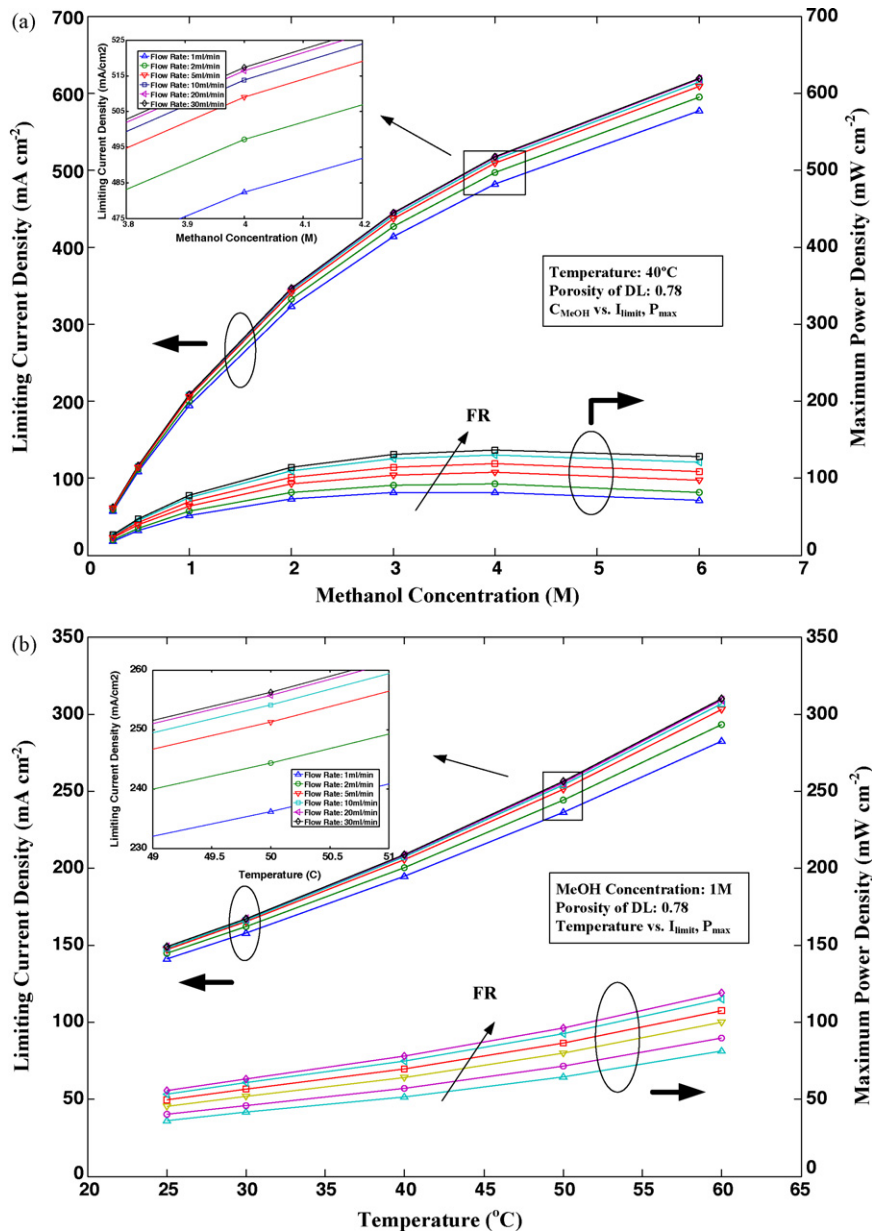
Fig. 9. Influence of operating parameters on DMFC limiting current density and maximum power output (a) input methanol concentration increases from 0.25 up to 6 M; (b) operating temperature increases from 25 to 60 °C. Flow rate of methanol solution varies from 1 to 30 ml min^{-1} for both cases.

4.4. Flow-field structure

As mentioned earlier, the diffusion layer imposes a significant effect on the mass transport resistance in a DMFC. An investigation of its influence on cell limiting current density and maximum power density was carried out by changing the under-rib width and cross-section while keeping the same total active area and channel parallel number in the field. Fig. 8a depicts the results obtained from the modified flow-field structure. In the modification, the under-rib width between two adjacent channels was increased from 0.01 to 0.14 cm, while the cross-sectional area was kept constant at 0.075 cm × 0.075 cm. With the total flow-field area and channel parallel number unchanged, the contact length between the channel and diffusion layer then decreases from 0.1105 to 0.0455 cm. At the same time, the cross-sectional shape of each channel will also change. The change in cross-section of two adjacent channels with a connecting under-rib is given in Fig. 8a for a horizontal shape, square shape, and a vertical shape. Both the limiting current density and maximum power density reduce with the increasing under-rib width due to increased mass transport resistance. Since the mass-transfer at the channel|diffusion layer interface depends on the contact area and the diffusion flow mainly occurs underneath this open space, it is concluded that the performance degradation is primarily caused by inefficient mass-transfer and reduced diffuse flux. Even though the flow velocity in the channel does not change for constant cross-sectional area, the pressure difference between adjacent channels becomes higher with decreasing channel hydraulic number. The under-rib mass transport will then be enhanced by the increasing pressure. The contrasting contributions on cell performance from mass-transfer/diffusion and under-rib convection reveal that effective mass-transfer from the channel and its diffusion in the diffusion layer are dominating factors the optimum mass transport for electrochemical reaction. Given in the steep drop in limiting

current density, the drop in maximum power density in Fig. 8a is the result of heavy methanol crossover in the low mass-transport resistance region.

Another analysis is given in Fig. 8b with a similar structure modification as that in Fig. 8a while maintaining the channel height at 0.075 cm, as adopted in the experimental hardware, where the flow velocity in the channel increases with increasing under-rib width. The higher flow velocity results in more effective mass-transfer at the channel|diffusion layer interface. It also facilitates mass transport in the under-rib region by improving the pressure difference between adjacent channels. Therefore, the performance of the DMFC is promoted with a wider under-rib width. Nevertheless, the improvement is moderate as the contact area between the channel and diffusion layer shrinks quickly and thus limits the effective mass-transfer.

Both analyses show the influence of the open ratio in the flow-field channel regions for effective mass-transfer at the channel|diffusion layer interface and its diffusion flow. The reduced contact between the flow-field rib and diffusion layer also brings a high electrical resistance in electron transport. As a result, a trade-off should be considered to achieve an optimum flow-field design.

4.5. Influence of operating parameters

Variations in the limiting current density and maximum power density as functions of methanol concentration and temperature for different methanol flow rates are presented in Fig. 9a and b, respectively. For all cases, the limiting current densities increase with methanol flow rate at the anode. There is, however, no further, improvement at flow rates above 5 ml min^{-1}. A similar trend can also be observed for the power density, which changes moderately compared with that in the limiting current density. Under a slow flow rate, the low liquid velocity in the anode channel leads to a lower mass-transfer at the interface between the channel and diffusion layer. The pressure drop across the SSC is also smaller, and thus induces a weaker pressure that drives under-rib convection. Consequently, the under-rib mass transport is suppressed. As a result, the diffusion layer exhibits a higher-mass-transfer resistance against the methanol supply at the reaction sites. Although flow rate adjustment will improve the situation, a large increase in flow rate will bring no significant improvement in methanol transport due to the absence of sufficient fuel residence time.

The limiting current density is found to increase with higher methanol concentration. On the other hand, the increase in maximum power density becomes less remarkable after 2 M and drops at 6 M in Fig. 9a. The results indicate that the enhanced mass-transfer for electrochemical reactions due to increased input methanol concentration also makes the methanol crossover more severe and eventually results in a poor power density. By contrast, an increase in operating temperature facilitates an improvement in limiting current density and power density. Effective methanol transport is ensured under a high operating temperature because of its high diffusion coefficient. At the same time, the reaction kinetics are also improved, and the methanol crossover, which results from excess methanol without reaction, can be reduced. Overall, the control, of input methanol concentration has a more significant effect than the suppression of methanol crossover in achieving an improvement in DMFC performance.

5. Conclusion

In this study, a complexity-reduced mathematical model has been developed for a liquid-feed DMFC. The model involves two significant mass-transport phenomena, namely: (i) the two-phase transport effect due to carbon dioxide generation at the anode, and (ii) the under-rib mass convection effect in the presence of a pressure drop along a single serpentine fuel channel. This model provides a more realistic performance analysis of DMFC design. The results obtained from the model are in good agreement with experimental data. Thus, proposed model serves as a useful tool for the optimization of DMFC design and performance.

References

[1] J. Larminie, A. Dicks, Fuel Cell Systems Explained, John Wiley & Sons, England, 2003.
[2] W. Vielstich, H. Gasteiger, A. Lamm, Handbook of Fuel Cells—Fundamentals, Technology and Applications, vol. 1, John Wiley & Sons, New York, 2003.
[3] A.A. Kulikovsky, J. Electrochem. Soc. 152 (6) (2005) A1121–A1127.
[4] Q. Ye, T.S. Zhao, J. Electrochem. Soc. 152 (11) (2005) A2238–A2245.
[5] W.C. Choi, M.K. Jeon, Y.J. Kim, S.I. Woo, W.H. Hong, Catal. Today 93–95 (2004) 517–522.
[6] C.Y. Wang, Chem. Rev. 104 (2004) 4727–4766.
[7] C. Xu, Y.L. He, T.S. Zhao, R. Chen, Q. Ye, J. Electrochem. Soc. 153 (7) (2006) A1358–A1364.
[8] K. Scott, W.M. Taama, S. Kramer, P. Argyropoulos, K. Sundmacher, Electrochim. Acta 45 (1999) 945–957.
[9] J.P. Meyers, J. Newman, J. Electrochem. Soc. 149 (2002) A710–A717.
[10] J.P. Meyers, J. Newman, J. Electrochem. Soc. 149 (2002) A718–A728.
[11] J.P. Meyers, J. Newman, J. Electrochem. Soc. 149 (2002) A729–A735.
[12] S.F. Baxter, V.S. Battaglia, R.E. White, J. Electrochem. Soc. 146 (2000) 437–447.
[13] C.H. Chen, T.K. Yeh, J. Power Sources 160 (2006) 1131–1144.
[14] H. Yang, T.S. Zhao, Q. Ye, J. Power Sources 139 (2005) 79–90.
[15] P. Argyropoulos, K. Scott, W.M. Taama, Electrochim. Acta 44 (1999) 3575–3584.
[16] M.M. Mench, S. Boslet, S. Thynell, J. Scott, C.Y. Wang, Direct methanol fuel cells, in: S. Narayanan, T. Zawodzinski, S. Gottesfed (Eds.), The Electrochemical Society Proceedings Series, Pennington, NJ, 2001 (PV 2001-4, P.241).
[17] X.G. Yang, F.Y. Zhang, A.L. Lubawy, C.Y. Wang, Electrochem. Solid-State Lett. 7 (2004) A408–A411.
[18] Z.H. Wang, C.Y. Wang, J. Electrochem. Soc. 150 (4) (2003) A508–A519.
[19] Z.H. Wang, C.Y. Wang, K.S. Chen, J. Power Sources 94 (2001) 40–50.
[20] C.Y. Wang, P. Cheng, Adv. Heat Transfer 30 (1997) 93–196.
[21] E. Birgersson, J. Nordlund, M. Vynnycky, C. Picard, G. Lindbergh, J. Electrochem. Soc. 151 (2004) A2157–A2172.
[22] J. Divisek, J. Fuhrmann, K. Gartner, R. Jung, J. Electrochem. Soc. 150 (2003) A811–A825.
[23] J. Rice, A. Faghri, Int. J. Heat Mass Transfer 49 (2006) 4804–4820.
[24] W.W. Yang, T.S. Zhao, Electrochim. Acta 52 (2007) 6125–6140.
[25] W.P. Liu, C.Y. Wang, J. Electrochem. Soc. 154 (2007) B352–B361.
[26] C.Y. Soong, W.M. Yan, C.Y. Tseng, H.C. Liu, F.L. Chen, H.S. Chu, J. Power Sources 143 (2005) 36–47.
[27] Y. Wang, C.Y. Wang, J. Power Sources 147 (2005) 148–161.
[28] G. Inoue, Y. Matsukuma, M. Minemoto, J. Power Sources 162 (2006) 81–92.
[29] M.V. Williams, E. Begg, L. Bonville, H.R. Kunz, J.M. Fenton, J. Electrochem. Soc. 151 (2004) 1173–1189.
[30] J.G. Pharoah, J. Power Sources 144 (2005) 148–159.

[31] P.H. Oosthuizen, L. Sun, K.B. McAuley, Appl. Therm. Eng. 25 (2005) 1083–1096.
[32] C.H. Cheng, K. Fei, C.W. Hong, Comput. Chem. Eng. 31 (2007) 247–257.
[33] H. Guo, C.F. Ma, Electrochem. Commun. 6 (2004) 1131–1134.
[34] B.L. Garcia, V.A. Sethuraman, J.W. Weidner, R.E. White, R. Dougal, J. Fuel Cell Sci. Technol. 1 (2004) 43–46.
[35] X. Ren, T.E. Springer, T.A. Zawodzinski, S. Gottesfeld, J. Electrochem. Soc. 147 (2) (2000) 466–474.
[36] F.M. White, Fluid Mechanics, 4th edition, WCB/McGraw-Hill, New York, 1999.
[37] C.Y. Wang, Handbook of Fuel Cells—Fundamentals, Technology and Applications, vol. 3, John Wiley & Sons, New York, 2003, pp. 337–347.
[38] J.M. Smith, H.C. VanNess, M.M. Abbott, Introduction to Chemical Engineering Thermodynamics, McGraw-Hill, New York, 1996, p. 667.
[39] F.D. Incropera, D.P. DeWitt, Fundamentals of Heat and Mass Transfer, John Wiley & Sons, Inc., New York, 1985.
[40] C.L. Yaws, Handbook of Transport Property Data: Viscosity, Thermal Conductivity and Diffusion Coefficients of Liquids and Gases, Gulf Pub Co., Houston, TX, 1995.
[41] E.L. Cussler, Diffusion: Mass Transfer in Fluidic System, Cambridge University Press, New York, 1984.
[42] X. Ren, T.E. Springer, S. Gottesfeld, J. Electrochem. Soc. 147 (2000) 92–100.